Research Square

Preprints are preliminary reports that have not undergone peer review.
They should not be considered conclusive, used to inform clinical practice,
or referenced by the media as validated information.

Formation of Gradient Residual Stress in Ultrasonic Vibration-Assisted End Grinding Inconel 718: Microscopic Mechanism and Modeling

Wenhao Liu

liuwh666@126.com

Dalian University of Technology

Yan Bao
Xudong Guo
Xianglong Zhu
Renke Kang
Zhigang Dong

Research Article

Keywords: Thermo-mechanical behavior, Microstructure, Plastic deformation, Residual stress, Ultrasonic vibration-assisted end grinding

Posted Date: June 22nd, 2026

DOI: https://doi.org/10.21203/rs.3.rs-9623853/v1

License: This work is licensed under a Creative Commons Attribution 4.0 International License.
Read Full License

Formation of Gradient Residual Stress in Ultrasonic Vibration-Assisted End Grinding Inconel 718: Microscopic Mechanism and Modeling

Wenhao Liu[a], Yan Bao[a], Xudong Guo[a], Xianglong Zhu[a], Renke Kang[a], Zhigang Dong[a,] *

[a] *State Key Laboratory of High-Performance Precision Manufacturing, Dalian University of Technology, Dalian 116024, China*

*Corresponding author**:** Email address: dongzg@dlut.edu.cn (Zhigang Dong)

Abstract: Residual stress (RS) on machined surfaces critically influences in-service performance. However, the underlying microscopic physical mechanisms remain insufficiently understood. The plastic deformation behavior under different parameters in ultrasonic vibration-assisted end grinding (UVAEG) was systematically investigated by RS characterization, in-situ grinding force measurement, and subsurface microstructure observation. An evaluation method for RS on machined surfaces was proposed. A prediction model for RS on machined surfaces was established based on dislocation pile-up theory. The microscopic mechanism of RS formation was analyzed. The effects of spindle speed and grinding depth on plastic deformation depth and the formation of gradient RS were also systematically studied. The results show that surface RS is positively correlated with dislocation density. The residual stress induced by grinding primarily originates from local stress fields generated by microstructural defects within the material. A larger plastic deformation depth is favorable for the formation of a deeper RS affected layer. Lower spindle speed and larger cutting depth can generate higher grinding forces, thereby promoting dislocation multiplication and migration, increasing the degree of lattice distortion and the depth of the affected layer, and consequently resulting in higher residual stress and a deeper affected layer. This study elucidates the microscopic mechanisms underlying internal stress formation at machined surfaces and provides a theoretical basis for optimizing machining processes to control material performance effectively.

Keywords: Thermo-mechanical behavior; Microstructure; Plastic deformation; Residual stress; Ultrasonic vibration-assisted end grinding

1. Introduction

Inconel 718 is widely used in critical rotating components of aerospace engines due to its excellent mechanical properties, corrosion resistance, creep resistance, and fatigue performance [1, 2]. RS inevitably develops on machined surfaces [3], and RS on the machined surface plays a crucial role in the fatigue performance of components[4, 5]. Appropriate compressive RS can partially offset operational stresses [6, 7], suppress surface crack initiation, and shift fatigue crack origins from the surface to subsurface regions. Moreover, RS can influence crack propagation rates by altering the stress intensity factor [8–10]. Beyond fatigue performance, RS is also a critical factor affecting corrosion resistance [11], creep resistance [12], and dimensional stability [13].

RS within materials can be classified into two categories based on scale: macroscopic and microscopic RS [14]. Macroscopic RS generally exists across the bulk material and significantly influences overall performance, potentially causing part warping, deformation, or crack formation [15]. In contrast, microscopic RS manifests at the microstructural scale, comprising intergranular and intragranular RS [16]. Intergranular RS originates from differential plastic deformation among grains or from variations in thermal expansion and phase transformation responses. Intragranular RS arises from localized structural distortions within individual grains, such as dislocations, second-phase particles, or subgrain boundaries [17, 18]. Although numerical differences may exist between macroscopic and microscopic RS, they are not independent [19]. Macroscopic RS is typically considered as the superposition of microscopic RS across multiple grains [20]. Directional accumulation of heterogeneous stress fields within and among grains leads to the development of large-scale stresses and strains, which are strongly affected by microstructure. [21].

RS on the machined surface is generally regarded as macroscopic RS, formed by the combined action of mechanical and thermal stresses [22–24]. Its formation involves loading, unloading, and relaxation stages [25–27]. During loading, compression is induced by the contact between the tool and workpiece surface, while thermal gradients between the surface and interior can generate tensile stress [28]. Analytical methods based on elasticity effectively describe the influence of process parameters on RS [29]. Li et al. [30] investigated the effects of mechanical and thermal loads during grinding, calculating mechanical and thermal stresses induced by a single abrasive grain and determining RS on the machined surface through loading and unloading analysis. Some studies have demonstrated a positive correlation between RS on the machined surface and plastic deformation, whereby plastic deformation inhibits elastic strain recovery,

leading to RS formation. Ballard et al. [31] reported that laser peening induces severe plastic deformation at the surface, generating high compressive RS, and developed a predictive model based on stress wave theory. Finite element methods are also widely used to predict RS on the machined surface. Da et al. [32] developed an orthogonal cutting finite element model and analyzed thermo-mechanical variations under different cutting conditions, showing that increasing cutting speed, reducing uncut chip thickness, and decreasing tool edge radius favor compressive RS formation. Jiang et al. [33] proposed a dynamic force direction transformation method for planar milling, constructing a multi-process coupled finite element model that successfully predicted RS in thin-walled aerospace components and quantified contributions from different processes.

Although previous studies have qualitatively and numerically explained the formation of RS on the machined surface from a macroscopic mechanics perspective, the underlying microscopic physical origins remain unclear. In particular, how microstructural evolution induced by changes in processing conditions influences macroscopic RS distribution across scales is yet to be systematically elucidated. To address these issues, surface RS characterization, grinding force measurement, and microstructure observation were combined in this study. The grinding force, RS, and dislocation density under different process parameters were systematically analyzed. Based on this analysis, the microstructure evolution governed by plastic deformation under different process parameters was revealed. By integrating multi-scale microstructural characterization with RS measurements, quantitative relationships among RS on the machined surface, dislocation density distribution, and plastic deformation depth were established. Furthermore, a defect-elasticity retardation-based theory and predictive model for RS formation were proposed, elucidating the intrinsic physical mechanisms of RS on the machined surface from the perspective of micro-defect evolution and elastic strain retention.

2. Materials and experiments

2.1. Materials

The specimens used in the present machining experiments were solution-annealed Inconel 718 superalloy, with Ni, Cr, and Fe as the principal alloying elements. Fig. 1(a) illustrates the initial grain structure of the material, in which the grain size predominantly ranges from 0 to 10 μm. The maximum grain size does not exceed 35 μm, and the average grain size is 20.22 μm. The grains are mainly equiaxed, and a small number of annealing twins can be observed within some of the larger grains. Fig. 1(b) presents the kernel average misorientation (KAM) map of the material. Overall, the local misorientation within the grains is relatively low, whereas higher KAM values are observed near grain boundaries compared to intragranular regions, indicating the presence of weak localized strain in the vicinity of grain boundaries. Fig. 1(c) shows the lattice strain measured under different X-ray incident angles. Based on the relationship between lattice strain and incident angle, the initial RS within the material was calculated to be −302.1 ± 15.9 MPa..

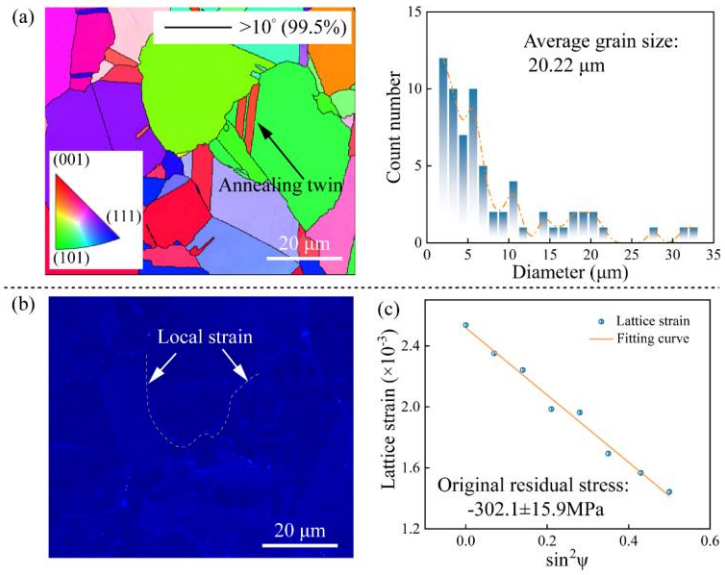


Fig. 1. Material characteristics of Inconel 718 superalloy: (a) grain size and morphology, (b) KAM, and (c) lattice strain and original RS

2.2. Mechanical processing method

As shown in Fig. 2, ultrasonic vibration device is mounted beneath the spindle, and the grinding wheel is fixed to the ultrasonic vibration system. The electrical signal generated by the ultrasonic power supply is

transmitted to the transducer through a non-contact power transmission mode, where it is converted into a high-frequency vibration signal. The vibration signal is further amplified by the horn and finally delivered to the grinding wheel, thereby realizing ultrasonic vibration-assisted end grinding. The ultrasonic vibration amplitude is approximately 4 μm, and the vibration frequency can reach up to 25 kHz. A high-strength resin-bonded grinding wheel was employed in the experiments, with a wheel diameter of 20 mm and an abrasive grain concentration of 100.

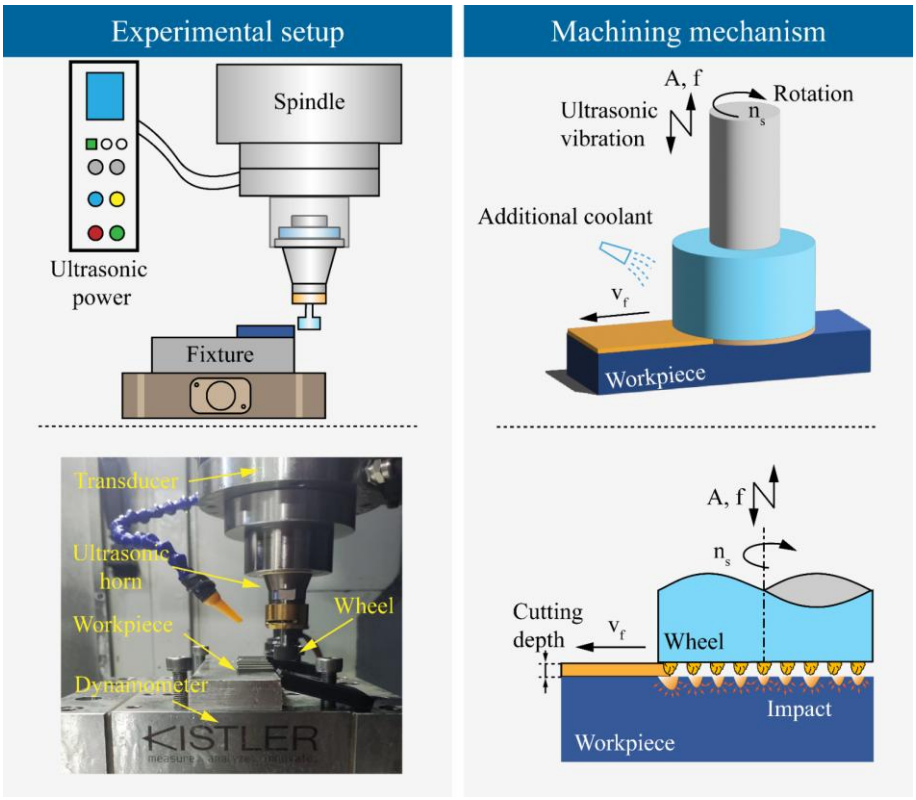


Fig. 2. Experimental Setup and Mechanism of UVAEG

Table 1

Experimental scheme for UVAEG

Groups	Spindle speed (rpm)	Cutting Depth (μm)	feed rate (mm/min)
1	1000	30	60
2	2000	30	60
3	3000	30	60
4	4000	30	60
5	2000	20	60
6	2000	40	60

Plate-shaped Inconel 718 superalloy specimens were prepared by wire electrical discharge machining and cut into dimensions of 25 × 6 × 3 mm. The specimens were fixed onto the dynamometer using high-

strength adhesive and mechanical fixtures. Grinding force signals in different directions during machining were acquired using dynamometer, with a constant sampling frequency of 10 kHz and a sampling duration of 40 s. Since slight inclination of the machined surface may occur after specimen clamping, a pre-grinding process with fixed machining parameters was conducted before each grinding test to ensure surface flatness and consistency of the cutting depth. As listed in Table 1, the UVAEG experiments were divided into six groups, while the grinding wheel feed speed was maintained at 60 mm/min for all tests. During grinding, a water-based coolant with a flow rate of 12 L/min was applied to cool the machining zone.

2.3. Measurements and Characterization

RS was measured using the $\sin^2\psi$ method. A Cr target was employed as the X-ray source, operated at an accelerating voltage of 26 kV and a tube current of 6 mA. The collimator diameter was set to 2 mm. Measurements were conducted on the {311} diffraction plane at a diffraction angle of 149°. The strain method was used to calculate RS, with a stress constant of 6.5. The depth profile of RS was determined by electrolytic polishing, which is widely regarded as an effective technique for RS depth analysis. A saturated NaCl solution with a mass concentration of 3.5% was used as the electrolyte. After each polishing step, the removed layer thickness was measured using a micrometer gauge. The surface morphology of the machined surface was characterized using a white-light interferometer. Surface and subsurface microstructures were analyzed using electron backscatter diffraction (EBSD). In addition, transmission electron microscopy (TEM) was employed to further investigate machining-induced subsurface microstructural evolution. TEM specimens with a thickness of approximately 5 μm were prepared using a focused ion beam (FIB) technique.

3. Results

3.1. RS on the machined surface

Fig. 4(a) presents the measured RS on the machined surface at different spindle speeds and cutting depths. At a spindle speed of 1000 rpm, the surface RS was −866.3 ± 28.9 MPa. As the spindle speed increased to 4000 rpm, the surface RS decreased to −471.6 ± 29.7 MPa. Under the same spindle speed, when the cutting depth was 20 μm, the surface RS was −437.8 ± 32.5 MPa; increasing the cutting depth to 40 μm resulted in a surface RS of −793.8 ± 20.3 MPa. As shown in Fig. 4(b-d), the depth profiles of RS reveal a spoon-shaped distribution in the subsurface region, where the RS initially increases and then decreases from the surface to the bulk. At a spindle speed of 2000 rpm and a cutting depth of 30 μm, the

maximum RS occurred at a depth of 27.93 μm, and the depth of the compressive RS layer was 78.3 μm. When the spindle speed increased to 3000 rpm, the maximum RS shifted to 19.73 μm, and the compressive RS layer decreased to 71.6 μm. For a cutting depth of 40 μm, the maximum RS appeared at 28.57 μm, and the compressive RS layer depth increased to 84.8 μm. These experimental results indicate that a lower spindle speed and a larger cutting depth are favorable for obtaining higher surface RS and a deeper compressive RS layer.

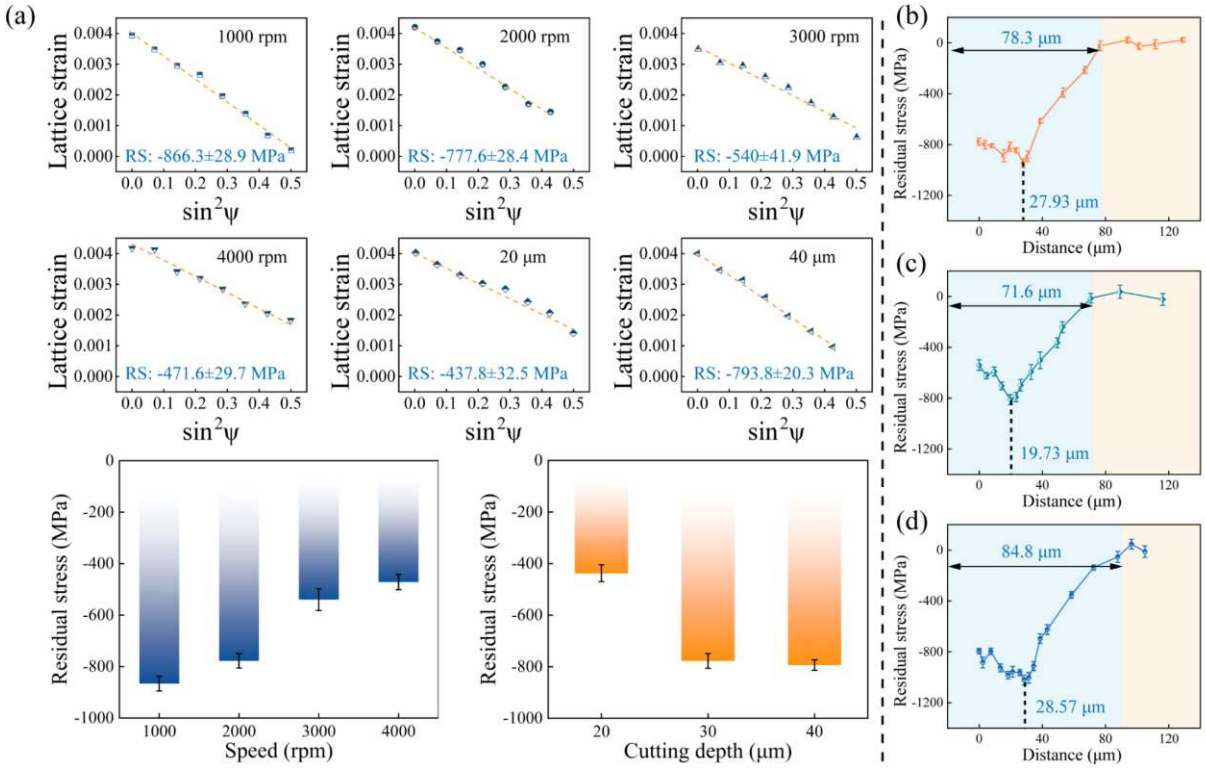


Fig. 4 RS on machined surface during UVAEG: (a) Variation of surface RS with spindle speed and cutting depth. (b) Subsurface RS distribution at a spindle speed of 2000 rpm and a cutting depth of 30 μm. (c) Subsurface RS distribution at a spindle speed of 3000 rpm and a cutting depth of 30 μm. (d) Subsurface RS distribution at a spindle speed of 2000 rpm and a cutting depth of 40 μm.

3.2. Grinding Force in UVAEG

Fig. 5 presents the real-time measurements of grinding forces at different spindle speeds. As shown in Fig. 5(a), the measured grinding force can be divided into the wheel entry stage, the steady-state cutting stage, and the wheel exit stage. It is noteworthy that during the steady-state cutting stage, the tangential force exhibits minor fluctuations at spindle speeds between 1000 and 3000 rpm, whereas the instantaneous grinding force shows increased fluctuations when the spindle speed is raised to 4000 rpm. Fig. 5(b)

illustrates the real-time normal grinding force. At 1000 rpm, the average normal grinding force is significantly higher than those measured at other speeds, and its fluctuation amplitude is also notably larger. The average grinding forces at different spindle speeds were statistically analyzed, as shown in Fig. 5(c). Overall, both the average normal and tangential grinding forces decrease progressively with increasing spindle speed, and the decay rate of grinding force diminishes at higher speeds. At 1000 rpm, the average normal force is 20.12 ± 0.91 N. When the spindle speed is increased to 2000 rpm, the average normal force rapidly decreases to 9.62 ± 0.52 N, corresponding to a force reduction of approximately 52.2%. As the spindle speed further increases to 3000 rpm, the average normal force drops to 6.34 ± 0.16 N. Finally, at 4000 rpm, the average normal and tangential forces decrease to 5.94 ± 0.31 N and 3.42 ± 0.29 N, respectively, with the reduction rate compared to 3000 rpm being only 6.3%.

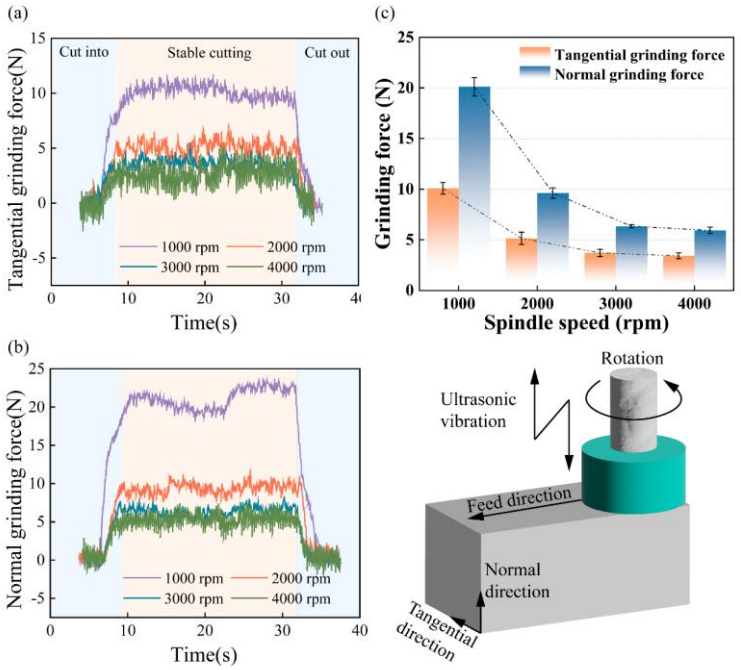


Fig. 5. Grinding force measurements at different spindle speeds. (a) Real-time tangential grinding force. (b) Real-time normal grinding force. (c) Variation of average grinding forces with spindle speed.

As shown in Fig. 6(a), the tangential grinding force exhibits periodic fluctuations during the steady-state cutting stage. Interestingly, at cutting depths of 20 μm and 30 μm, the tangential force remains relatively stable over time, whereas at a cutting depth of 40 μm, the tangential force shows a slight decreasing trend with time. Fig. 6(b) illustrates the variation of the normal grinding force at different cutting depths. At a shallow cutting depth of 20 μm, the normal force shows no significant change. However, when the cutting depth increases to 30 μm and 40 μm, the amplitude of instantaneous force fluctuations markedly

increases. Fig. 6(c) shows the variation of the average normal and tangential forces with cutting depth. At cutting depths of 20 μm, 30 μm, and 40 μm, the average normal forces are 5.15±0.34 N, 9.62±0.52 N, and 10.86±0.81 N, respectively. The growth rates of the average normal force with increasing cutting depth are 86.8% and 12.9%.

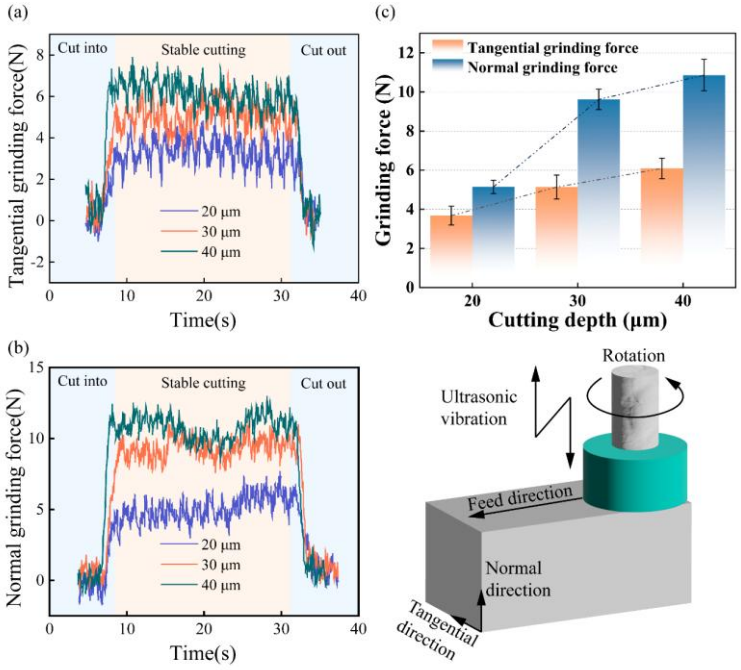


Fig. 6 Grinding force measurements at different cutting depths. (a) Real-time tangential grinding force. (b) Real-time normal grinding force. (c) Variation of average grinding forces with cutting depth.

3.3. Microstructural characteristics of the machined surface in UVAEG

As shown in Fig. 7， the dominant phase in the Inconel 718 superalloy is γ phase, which preferentially grows along the (111), (200), (220), and (311) crystallographic planes. Among them, γ phase exhibits the highest diffraction intensity on (111) plane. As shown in Fig. 7(a), variations in grinding speed did not lead to the appearance of new diffraction peaks, indicating that no phase transformation occurred during the UVAEG. However, the combined mechanical and thermal loads imposed during machining induced noticeable changes in both the position and intensity of the diffraction peaks. A magnified view of the (111) diffraction peak reveals that the peak intensity gradually increased with increasing grinding speed, while the corresponding diffraction angle shifted toward lower values. Statistical analysis of the full width at half maximum (FWHM) and peak position indicates that both parameters exhibit a correlated trend with respect to grinding speed. At a grinding speed of 1000 rpm, the FWHM of the machined surface was measured to be 0.532, with a diffraction angle of 43.74°. As the grinding speed increased to 4000 rpm, the FWHM

decreased to 0.405, accompanied by a leftward shift of the diffraction angle to 43.58°. As shown in Fig. 7(b), variations in cutting depth also resulted in peak broadening and peak position shifts. When the cutting depth increased from 20 μm to 40 μm, the FWHM increased from 0.402 to 0.451, while the diffraction angle shifted rightward from 43.59° to 43.67°. Similarly, the evolution trends of FWHM and diffraction angle with increasing cutting depth were found to be positively correlated.

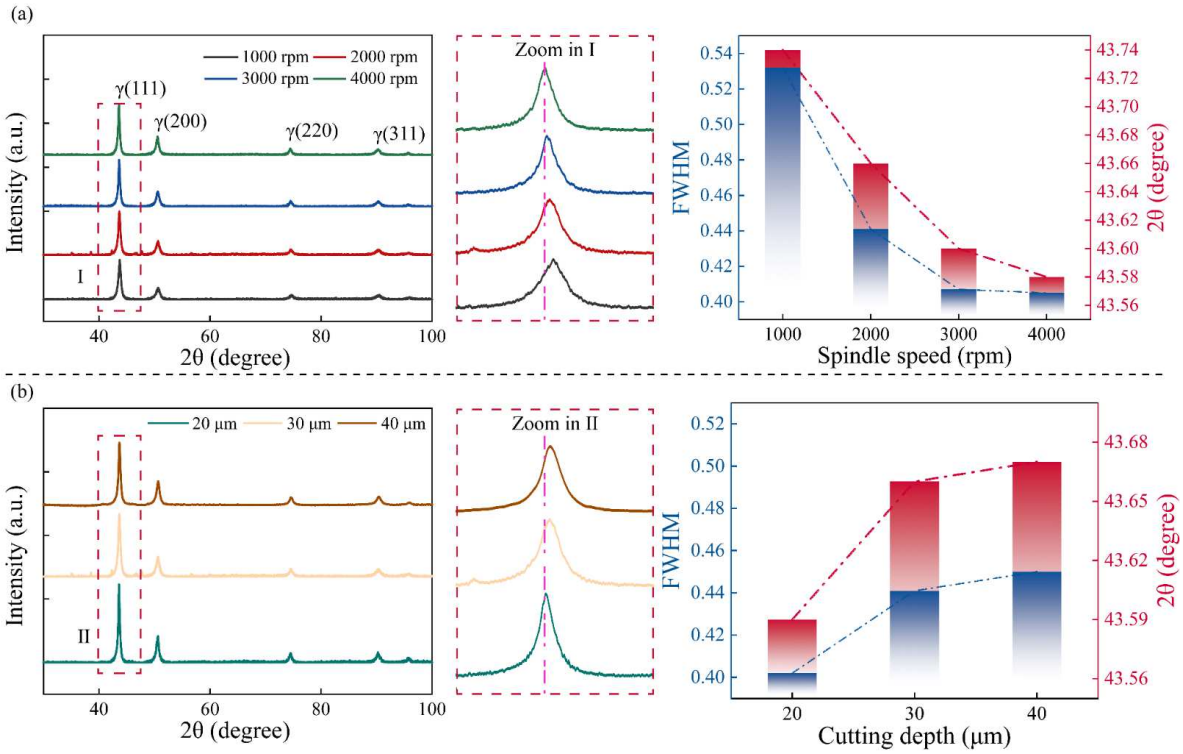


Fig. 7. XRD patterns of the machined surface after UVAEG: (a) evolution of diffraction peaks under different grinding speeds; (b) evolution of diffraction peaks under different cutting depths.

Fig. 8 illustrates the distribution characteristics of geometrically necessary dislocation (GND) and grain boundaries in the subsurface region under different processing parameters. As shown in Fig. 8(a), at a spindle speed of 2000 rpm and a cutting depth of 40 μm, the GND-affected layer extended to a depth of 8.13 μm. Meanwhile, a pronounced enrichment of low-angle grain boundaries (LAGBs) was observed near the machined surface, accounting for 12.6% of total grain boundaries. When the spindle speed was increased to 3000 rpm, the depth of the GND-affected layer decreased to 4.75 μm, accompanied by a reduction in the fraction of LAGBs to 9.9%, as shown in Fig. 8(b). In contrast, when the cutting depth was increased to 40 μm, the GND-affected depth significantly increased to 10.83 μm, and the LAGB fraction rose to 13.0% (Fig. 8(c)). Fig. 8(d) presents the depth profiles of the average geometrically necessary dislocation density (ρ_{GND}) under different processing conditions. In all cases, ρ_{GND} exhibited a rapid decay from the machined surface toward the bulk material. At a spindle speed of 2000 rpm and a cutting depth of

30 μm, the surface ρ_{GND} reached 17.7 × 10^{15} m^{-2}. When the cutting depth was increased to 40 μm, the highest surface ρ_{GND} was obtained, together with the slowest decay rate along the depth direction. By contrast, increasing the spindle speed to 3000 rpm resulted in a pronounced reduction in surface $\rho_{GND_}$ to 11.78 × 10^{15} m^{-2}. These results indicate that increasing the spindle speed suppresses dislocation accumulation and subgrain boundary formation, thereby reducing the depth of the plastically deformed layer. Conversely, increasing the cutting depth intensifies near-surface plastic deformation, leading to a higher dislocation density and enhanced formation of low-angle grain boundaries.

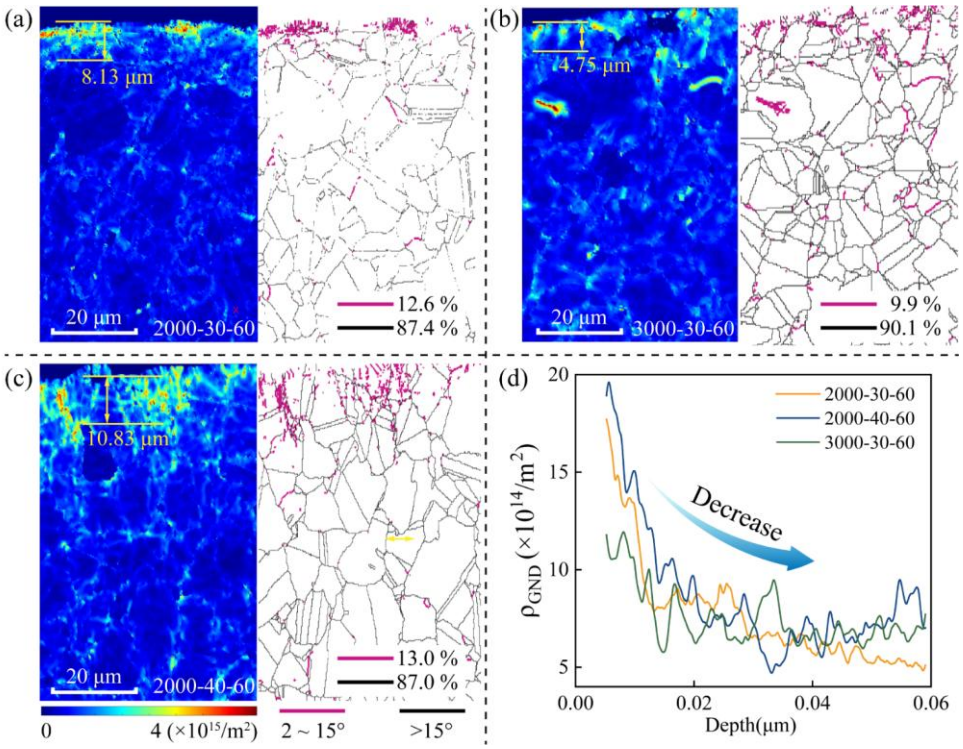


Fig. 8. Distribution characteristics of GND and grain boundaries in subsurface region: (a) spindle speed of 2000 rpm and cutting depth of 30 μm; (b) spindle speed of 3000 rpm and cutting depth of 30 μm; (c) spindle speed of 2000 rpm and cutting depth of 40 μm; (d) depth profiles of the average geometrically necessary dislocation density.

The introduction of ultrasonic vibration induces more severe plastic deformation on the machined surface and gives rise to a depth-dependent gradient microstructure in the subsurface region. To elucidate the subsurface microstructural characteristics, TEM characterization was performed on specimen #2. As shown in Fig. 9a), the overall subsurface microstructure can be clearly divided into three distinct regions from the surface toward the bulk: a grain-refined layer, a transition layer, and a plastic flow layer. Elongated δ phases were observed along the grain boundaries. The grain-refined layer exhibited a thickness of approximately 1.12 μm and was characterized by nanometer-sized equiaxed grains. The corresponding

selected area electron diffraction (SAED) pattern in Fig. 9(b) displays pronounced diffraction rings, indicating significant grain refinement, highly randomized crystallographic orientations, and intense plastic deformation in this region. The transition layer possessed a thickness of approximately 0.86 μm, in which the refined grains were relatively coarser.

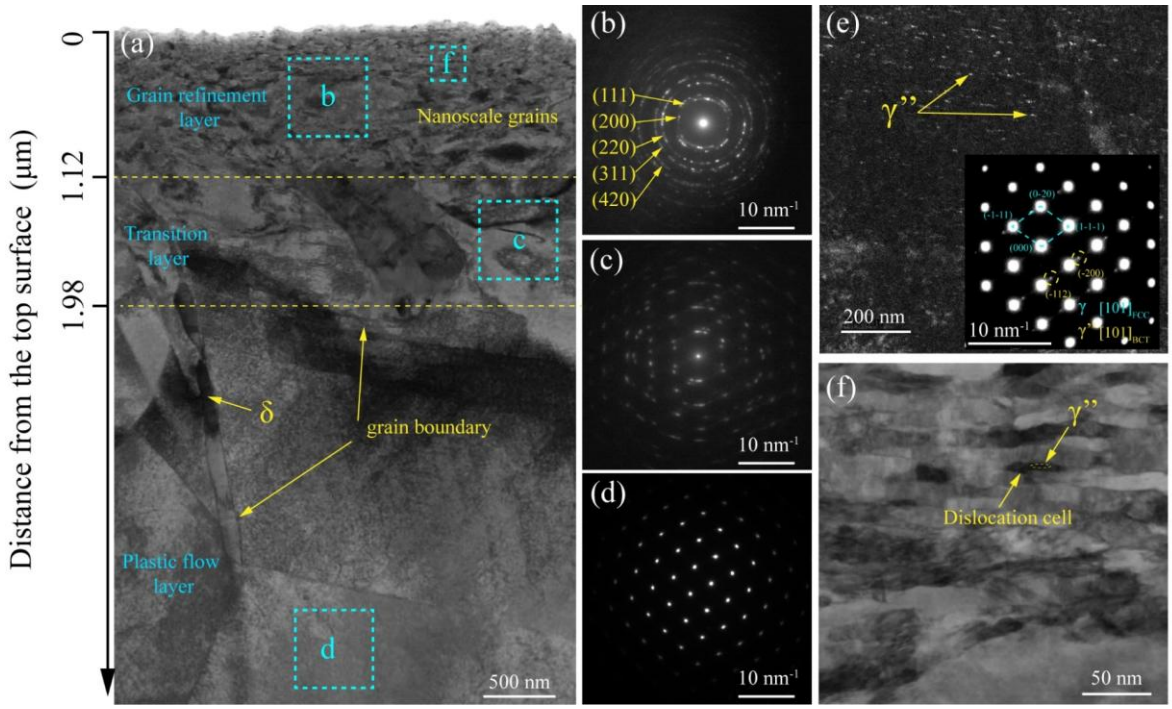


Fig. 9. TEM images of the gradient microstructure: (a) overall morphology of the subsurface region; (b–d) selected area electron diffraction (SAED) patterns at different depths from the machined surface; (e) distribution of γ″ phase within matrix; (f) γ″/dislocation composite structures.

As shown in the SAED pattern in Fig. 9(c), multiple diffraction spots were observed, while the ring features were less pronounced. This suggests that moderate plastic deformation occurred in this region, without inducing substantial crystallographic misorientation between adjacent grains. In the plastic flow layer, pronounced dislocation pile-ups were observed along the grain boundaries, while the grain size remained relatively large. The SAED pattern in Fig. 9(d) exhibited a typical single-crystal diffraction feature, indicating that only slight plastic deformation occurred in this region and that no evident dynamic recrystallization was activated. Fig. 9(e) shows the γ'' phase dispersed within the matrix, with its corresponding SAED pattern confirming the characteristic diffraction features of the γ'' phase. Additionally, cellular dislocation structures were observed in the vicinity of the γ'' precipitates, as shown in Fig. 9(f). This observation indicates that during the UVAEG process, dislocation motion was strongly impeded by the γ'' phase, leading to dislocation entanglement and the formation of γ''/dislocation composite structures. Such

interactions effectively promote dislocation accumulation near the machined surface, thereby contributing to the increased surface dislocation density.

4. Discussion

4.1. Relationship between RS on machined surface and microstructural evolution

In mechanical machining, microstructural evolution within the material is predominantly governed by the generation, motion, and rearrangement of dislocations, as well as the evolution of grain boundaries. The grain boundaries formed on the machined surface are generally attributed to continuous dynamic recrystallization [34], which, to a large extent, can be regarded as a manifestation of the evolution of dislocation configurations [35]. Consequently, variations in dislocation density and dislocation structures constitute the primary microstructural changes induced during machining. As discussed in Section 3.3, pronounced peak shifts and peak broadening were observed in the XRD patterns of the machined surface under different processing parameters (Fig. 7). Statistical analysis revealed a positive correlation between the evolution trends of FWHM and diffraction peak position. It is well established that an increase in FWHM reflects an elevated density of crystalline defects, such as dislocations and grain boundaries. Meanwhile, according to Bragg's diffraction law, a rightward shift of the diffraction peak indicates lattice contraction induced by compressive RS, with a larger peak shift corresponding to a higher magnitude of compressive RS [36]. Therefore, the consistency between diffraction peak broadening and peak shifting strongly suggests that the macroscopic variation of RS is intrinsically associated with changes in dislocation density.

As shown in Fig. 10, owing to the cutting characteristics associated with the negative rake angle of the abrasive grain, surface atoms are forced into the substrate under compressive stress, and elastic–plastic deformation is thereby induced in the machining zone [37]. From the perspective of microstructural defect evolution, such conditions of high strain and high strain rate substantially reduce the energy barrier for dislocation nucleation, thereby promoting dislocation emission, multiplication, and glide. Consequently, a high density of dislocations is introduced within the machined surface and its adjacent subsurface region, exhibiting a pronounced gradient distribution along the depth direction. Since these dislocations primarily originate from lattice mismatch and localized strain concentration caused by the inward embedding of surface atoms, the resulting non-equilibrium defect accumulation leads to compressive lattice distortion,

manifested as a reduction in interplanar spacing. Upon unloading, material regions that previously experienced elastic deformation tends to recover toward their original configurations. However, the elastic recovery process is significantly constrained by the long-term retention of dislocations, dislocation tangles, and other crystal defects introduced during machining. As a result, a portion of the elastic strain is retained and effectively "frozen" within the material.

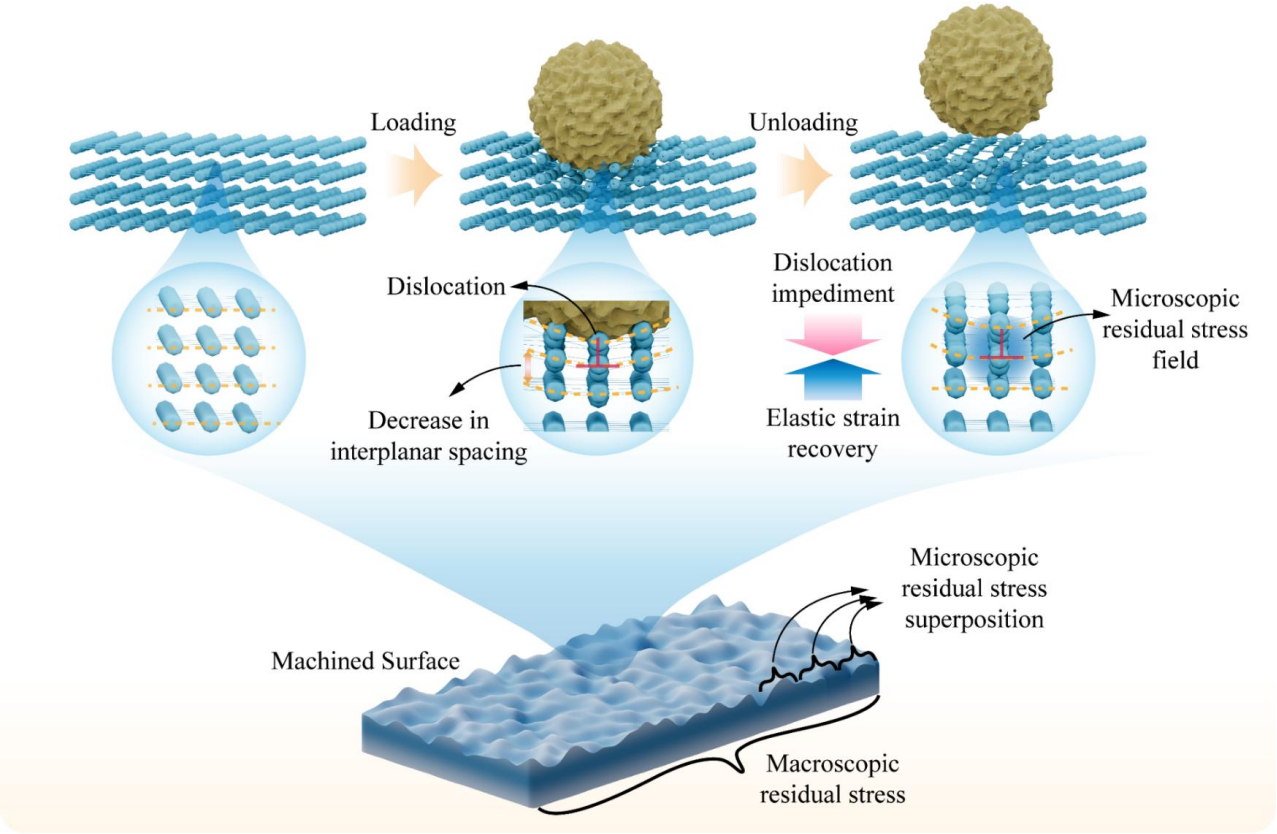


Fig. 10. Microscopic mechanism of RS formation on the machined surface

At the microscopic scale, dislocations—acting as line defects with long-range elastic stress fields—impede lattice relaxation through their elastic interactions and spatial arrangements, preventing the complete release of local elastic deformation. When the elastic recovery driving force reaches mechanical equilibrium with the pinning and blocking effects imposed by dislocations and other defects, a stable state of microscopic residual internal stress is established within the material. This phenomenon has been well documented in classical dislocation elasticity theory and experimental observations [38]. With the progressive accumulation and superposition of retained elastic strains of identical sign and orientation within the machining-affected region, these microscale stress fields undergo cooperative evolution and ultimately manifest as measurable macroscopic RS and deformation at larger length scales.

Macroscopic RS can be regarded as the spatial superposition of the internal stresses in multiple grains

within a given region[39]. The distribution of the internal stress field is strongly governed by the type and arrangement of dislocations. In the grinding surface layer, a significant plastic strain gradient is usually produced. To satisfy local deformation compatibility and lattice curvature requirements, dislocations are more likely to accumulate in the form of GND walls. Therefore, the formation of grinding-induced RS is mainly associated with the long-range stress field σ_{GND} retained by the GND walls. According to dislocation pile-up theory, σ_{GND} can be expressed as[39]:

$$\sigma_{\mathrm{GND}}(x) \sim \frac{GN|\vec{b}|}{2\pi(1-\nu)R} \tag{1}$$

where $|\vec{b}|$ is the magnitude of the Burgers vector, and R is the distance from the dislocation structure, which is larger than the dislocation core scale. Macroscopic RS can be treated as the average retained value after the superposition of local long-range stress fields over a given spatial scale. Thus, RS at a depth of z within the representative thin-layer volume element V_{z} can be expressed as:

$$\bar{\sigma}_{\mathrm{res}}(z) = \frac{1}{V}\int_{V} \sigma_{\mathrm{GND}} \mathrm{d}V \approx \frac{G|\vec{b}|}{2\pi(1-\nu)RV_z}\int_{V_z} N \mathrm{d}V \tag{2}$$

considering that the effective dislocation number is proportional to the local GND density, i.e., $N \propto \rho_{GND}$, the above equation can be further written as:

$$\bar{\sigma}_{\mathrm{res}}(z) \approx \frac{G|\vec{b}|}{2\pi(1-\nu)VR}\int_{V_z} \rho_{GND} \mathrm{d}V \tag{3}$$

the average GND density within the thin layer at the same depth is defined as Eqs. (4).

$$\bar{\rho}_{GND}(z) = \frac{1}{V_z}\int_{V_z} \rho_{GND} \mathrm{d}V \tag{4}$$

RS is not determined only by the local GND density. A long-range stress field is generated by the GND walls. Its influence range is usually larger than the spacing between adjacent GND walls. Therefore, the RS at depth z should also be regarded as a nonlocal superposition of the long-range stress contributions from neighboring regions along the depth direction. To reflect this spatial averaging effect and to avoid the singularity at R=0, a kernel function ψ is introduced to describe stress attenuation along the depth direction.

$$\psi = \exp(-\alpha_R z) \tag{5}$$

Where α_{R} is an adjustable parameter. It is used to control the decay rate of the exponential function. It should be noted that, by comparing the subsurface GND and RS distributions in Fig. 4 and Fig. 8, it can be

found that the highest dislocation density is located in the topmost surface region, but the maximum compressive RS is not located at the surface. Instead, it is located in the subsurface region. This phenomenon can be attributed to the combined effects of the following factors. First, significant plastic relaxation and free-surface effects are experienced by the topmost surface region. As a result, part of the elastic strain is released during unloading[40]. Second, strong dislocation annihilation, rearrangement, and cell structure formation occur in the surface region. Thus, the dislocation contribution that can effectively generate a long-range elastic stress field is weakened[41]. To describe the RS distribution along the depth direction, a distribution function Φ is introduced to characterize the gradient variation of RS along the depth direction:

$$\Phi = K_R \cos\left(\beta_R z + \lambda_R L_p^{\omega_R}\right) \tag{6}$$

where K_R is a parameter used to adjust the magnitude, β_R, λ_R, and ω_R are parameters used to regulate the gradient distribution. By combining Eqs. (3), (4), (5), and (6), the gradient distribution function of RS can be obtained as:

$$\bar{\sigma}_{\text{res}} = \frac{GK_R\bar{\rho}_{GND}\,|\vec{b}\,|}{2\pi(1-\nu)}\exp\left(-\alpha_R z\right)\cos\left(\beta_R z + \lambda_R L_p^{\omega_R}\right) \tag{7}$$

4.2. Plastic Deformation Layer Depth in UVAEG

The degree and depth of plastic deformation on the machined surface are both influenced by the applied thermo-mechanical loads. The grinding force is positively correlated with the material removal volume of a single abrasive grain per unit time. Section 3.2 demonstrated the influence of spindle speed and cutting depth on grinding force. As the spindle speed increases, the number of abrasive grains involved in material removal per unit time rises, resulting in a decrease in the material removal volume per single grain, which leads to a reduction in grinding force. In contrast, an increase in cutting depth directly increases the material removal volume, thereby increasing the grinding force. As shown in Fig. 11, the load applied by abrasive grains on the workpiece surface can be divided into mechanical stress and thermal stress components. Both the mechanical stress and thermal stress generated by the applied thermo-mechanical loads are related to the grinding force.

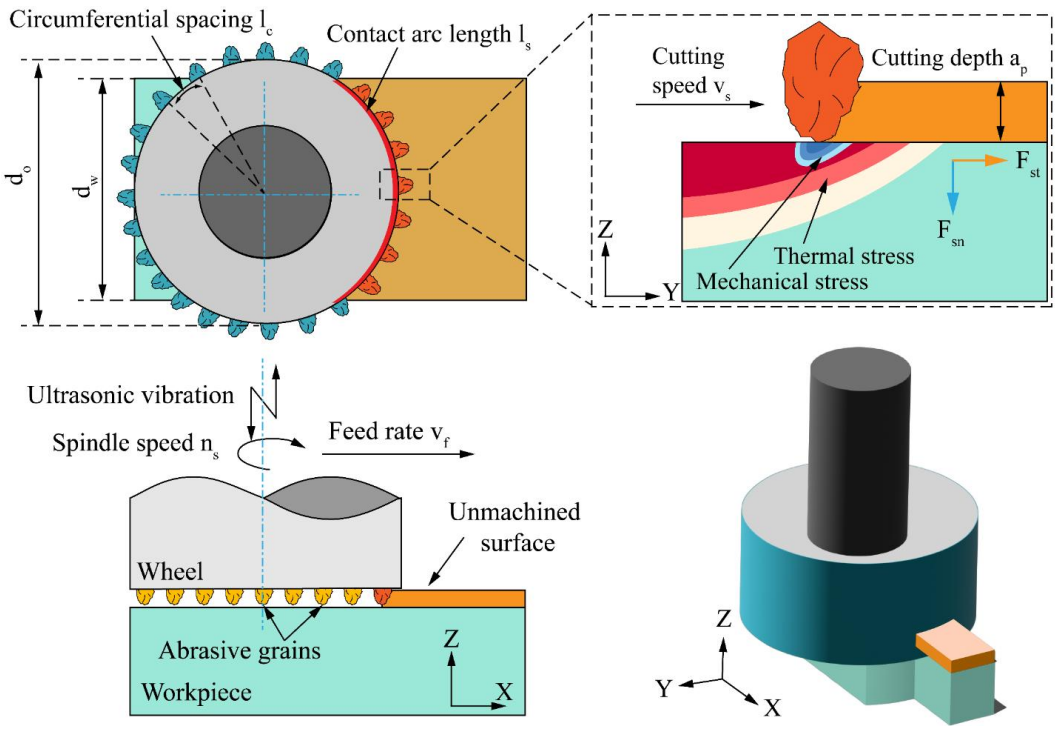


Fig. 11. Stress field generated by abrasive grain during UVAEG

The total grinding force during the UVAEG process is provided by all participating abrasive grains. The grinding force acting on a single abrasive grain can be expressed as:

$$\begin{cases} F_{sn} = \dfrac{F_n}{N} \\ F_{st} = \dfrac{F_t}{N} \end{cases} \tag{8}$$

where F_n and F_t are the total normal and tangential grinding forces, respectively, and N is the number of abrasive grains in contact with the workpiece.

$$N = \frac{l_s}{l_c} \tag{9}$$

Where l_c is the distance between adjacent abrasive grains along the circumference of the grinding wheel, and l_s is the contact arc length between the abrasive grains on the wheel end face and the workpiece. Assuming that the abrasive grains are uniformly distributed within the grinding wheel, the inter-grain distance can be calculated based on the grain concentration, grain size, and material density of the abrasive grains [42].

$$l_c = \left(\frac{C_a}{100} \frac{0.88 \times 10^{-6}}{\rho_g \pi d_g^{\,3} / 6} \right)^{-1/3} \tag{10}$$

where C_a is the concentration of cBN abrasive grains in the grinding wheel, ρ_g is the material density

of the abrasive grains, and d_g is the grain size. The contact arc length l_s can be calculated based on the geometric contact relationship between the grinding wheel and the workpiece.

$$l_s = d_o \arcsin\left(\frac{d_w}{d_o}\right) \tag{11}$$

Where d_o is the outer diameter of the grinding wheel, and d_w is the width of the workpiece.

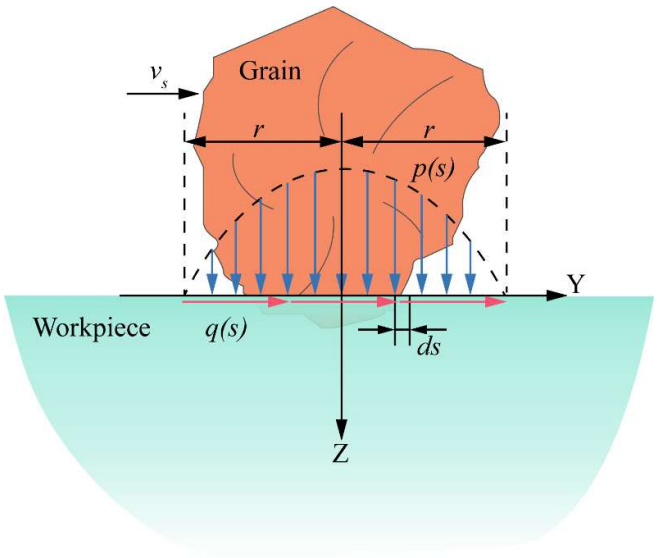


Fig. 12. Analytical diagram of mechanical stress calculated using Hertz contact theory.

In UVAEG, the mechanical interaction between abrasive grains and the workpiece surface can be conceptualized as a rolling-sliding contact problem [43]. The abrasive grain is simplified as a semi-infinite cylindrical roller. Since the contact area between the abrasive grain and the workpiece is limited, the workpiece surface is simplified as a semi-infinite elastic body with boundaries [44]. As shown in Fig. 12, the mechanical stress distribution on the machined surface during UVAEG is solved based on Hertz contact theory [45]. The mechanical stress in UVAEG can be expressed as follows:

$$\begin{cases} \sigma_{yy}^{\text{mech}}(y,z) = -\dfrac{2z}{\pi}\displaystyle\int_{-r}^{r}\frac{p(s)(y-s)^2}{\left[(y-s)^2+z^2\right]^2}ds - \frac{2}{\pi}\int_{-r}^{r}\frac{q(s)(y-s)^3}{\left[(y-s)^2+z^2\right]^2}ds \\ \sigma_{zz}^{\text{mech}}(y,z) = -\dfrac{2z^3}{\pi}\displaystyle\int_{-r}^{r}\frac{p(s)}{\left[(y-s)^2+z^2\right]^2}ds - \frac{2z^2}{\pi}\int_{-r}^{r}\frac{q(s)(y-s)}{\left[(y-s)^2+z^2\right]^2}ds \\ \tau_{yz}^{\text{mech}}(y,z) = -\dfrac{2z^2}{\pi}\displaystyle\int_{-r}^{r}\frac{p(s)(y-s)}{\left[(y-s)^2+z^2\right]^2}ds - \frac{2z}{\pi}\int_{-r}^{r}\frac{q(s)(y-s)^2}{\left[(y-s)^2+z^2\right]^2}ds \\ \sigma_{xx}^{\text{mech}}(y,z) = \nu\left(\sigma_{yy}^{\text{mech}}(y,z)+\sigma_{zz}^{\text{mech}}(y,z)\right) \end{cases} \tag{12}$$

where $p(s)$ is the normal load distribution, $q(s)$ is the tangential load distribution, and r is half the length of the abrasive grain contact area. Since the maximum length of the abrasive grain contact area does not

exceed the grain diameter, r is assumed to be approximately equal to the radius of the abrasive grain. The load distribution in the contact area can be calculated based on the contact length and the normal and tangential forces generated by a single abrasive grain.

$$\begin{cases} p_0 = \dfrac{3F_{sn}}{2\pi r^2} \\ \tau = \dfrac{F_{st}}{\pi r^2} \\ p(s) = \left(1 - \dfrac{s^2}{r^2}\right) p_0 \\ q(s) = \mu p(s) \end{cases} \tag{13}$$

In addition to mechanical stress, thermal stress is also generated during grinding because the temperature at the machined surface is significantly higher than that inside the material. The thermal expansion of the surface layer therefore induces thermal stress in the underlying substrate. Grinding heat is mainly generated by shear deformation of the material. The maximum heat flux associated with shear deformation can be calculated from the tangential grinding force of a single abrasive grain and the linear velocity of grain motion [46]. A triangular heat source distribution is generally considered an appropriate representation of the grinding temperature field [47].

$$\begin{cases} q_m = R_w \dfrac{F_{st} v_s}{b_{sw} l_{sc}} \\ R_w = \left(1 + \dfrac{0.97 k_{cBN}}{\sqrt{r v_s (\lambda \rho C)}}\right) \\ l_{sc} = \sqrt{2 r a_p} \\ q = q_m \left(1 + \dfrac{y'}{r}\right) \end{cases} \tag{14}$$

Where R_w is the fraction of heat conducted into the workpiece, λ is the thermal conductivity of the material, k_{cBN} is the thermal conductivity of the abrasive grain, ρ is the density of Inconel 718, C is the specific heat capacity, l_{sc} is the contact length between the abrasive grain and the workpiece surface, and b_{sw} is the contact width. For a band-shaped moving heat source in a semi-infinite medium, the temperature field can be expressed as:

$$\begin{cases} T(y,z)=\dfrac{q}{\pi\lambda}\displaystyle\int_{-r}^{r} e^{\frac{-v_s(y-x')}{2\alpha}} K_0\left\{\frac{v_s\left[(y-y')^2+z^2\right]^{1/2}}{2\alpha}\right\}dy' \\ \alpha=\dfrac{\lambda}{\rho C} \\ K_0=\dfrac{1}{2}\displaystyle\int_0^{\infty}\frac{e^{\left(-\omega-\frac{u^2}{4\omega}\right)}}{\omega}d\omega \\ u=\dfrac{v_s}{2\alpha}\sqrt{(y-l_{sc}\cos\varphi)^2+z^2} \end{cases} \tag{15}$$

Where α is the thermal diffusivity, K_0 is the zeroth-order modified Bessel function of the second kind that is time-dependent, and φ is the shear angle. During the cutting process, the temperature rapidly decreases from several hundred degrees Celsius at the machined surface to near-ambient temperature in the bulk material. As a result, the temperature field within the workpiece exhibits a highly non-uniform gradient distribution, which inevitably induces non-uniform thermal stresses inside the material. The thermal stress can be calculated based on the cutting temperature field [48].

$$\begin{cases} \sigma_{yy}^{\text{therm}}(y,z)=-\dfrac{\alpha_w E}{1-2v}\displaystyle\int_0^{\infty}\int_{-\infty}^{\infty}\left[G_{yh}\frac{\partial T_{(y,z)}}{\partial y}(y',z')+G_{yv}\frac{\partial T_{(y,z)}}{\partial z}(y',z')\right]\mathrm{d}y'\mathrm{d}z' \\ +\dfrac{2z}{\pi}\displaystyle\int_{-\infty}^{\infty}\frac{p(t)(t-y)^2}{\left[(t-y)^2+z^2\right]^2}\mathrm{d}t-\frac{\alpha E\cdot T_{(y,z)}}{1-2v} \\ \sigma_{zz}^{\text{therm}}(y,z)=-\dfrac{\alpha_w E}{1-2v}\displaystyle\int_0^{\infty}\int_{-\infty}^{\infty}\left[G_{zh}\frac{\partial T_{(y,z)}}{\partial y}(y',z')+G_{zv}\frac{\partial T_{(y,z)}}{\partial z}(y',z')\right]\mathrm{d}y'\mathrm{d}z' \\ +\dfrac{2z^3}{\pi}\displaystyle\int_{-\infty}^{\infty}\frac{p(t)}{\left[(t-y)^2+z^2\right]^2}\mathrm{d}t-\frac{\alpha E T_{(y,z)}}{1-2v} \\ \tau_{yz}^{\text{therm}}(y,z)=-\dfrac{\alpha_w E}{1-2v}\displaystyle\int_0^{\infty}\int_{-\infty}^{\infty}\left[G_{yzh}\frac{\partial T_{(y,z)}}{\partial y}(y',z')+G_{yzv}\frac{\partial T_{(y,z)}}{\partial z}(y',z')\right]\mathrm{d}y'\mathrm{d}z' \\ +\dfrac{2z^2}{\pi}\displaystyle\int_{-\infty}^{\infty}\frac{p(t)(y-t)}{\left[(t-y)^2+z^2\right]^2}\mathrm{d}t \\ p(t)=\dfrac{\alpha_w E T_{(y=0,z=0)}}{1-2v} \end{cases} \tag{16}$$

Where α_w is the linear thermal expansion coefficient. During the grinding process, the total stress field induced by a single abrasive grain can be obtained by superposition of the mechanical stress and the thermal stress. The stress component in the X-direction can be calculated according to Hooke's law.

$$\begin{cases} \sigma_{yy} = \sigma_{yy}^{\text{mech}}(y,z) + \sigma_{yy}^{\text{therm}}(y,z) \\ \sigma_{zz} = \sigma_{zz}^{\text{mech}}(y,z) + \sigma_{zz}^{\text{therm}}(y,z) \\ \tau_{yz} = \tau_{yz}^{\text{mech}}(y,z) + \tau_{yz}^{\text{therm}}(y,z) \\ \sigma_{xx} = v\left(\sigma_{yy} + \sigma_{zz}\right) - \alpha_W ET \end{cases} \tag{17}$$

Assuming that the workpiece material is a homogeneous and isotropic medium with strain-rate-independent hardening behavior, yielding is governed by the von Mises yield criterion. When the von Mises equivalent stress exceeds the yield strength of the material, yielding occurs and plastic deformation is initiated [49].

$$\sigma_{vM} = \frac{1}{\sqrt{2}}\sqrt{\left(\sigma_{xx} - \sigma_{yy}\right)^2 + \left(\sigma_{yy} - \sigma_{zz}\right)^2 + \left(\sigma_{xx} - \sigma_{zz}\right)^2} \tag{18}$$

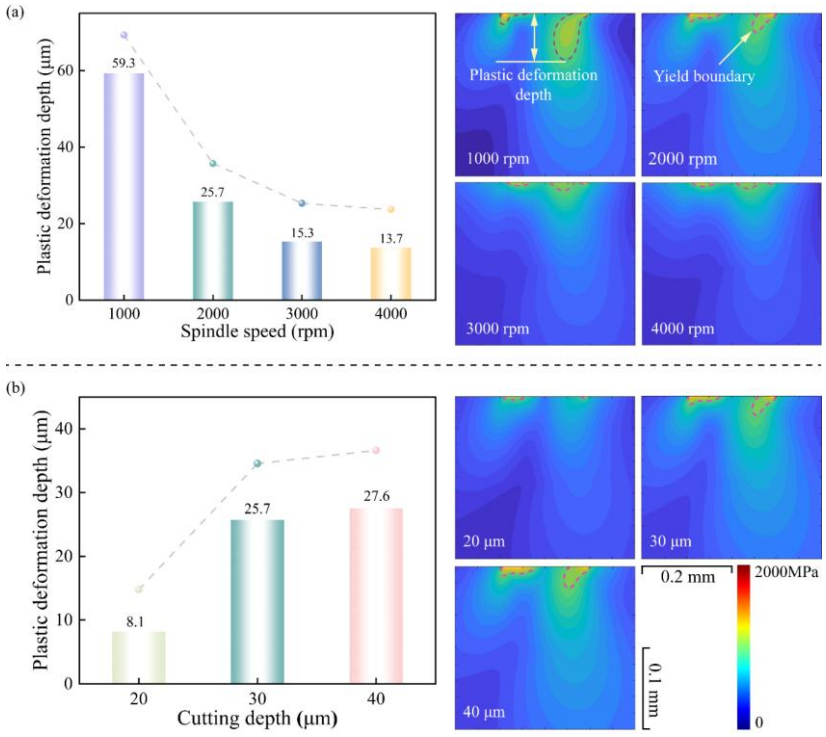


Fig. 13. Calculated plastic deformation depth under (a) different spindle speeds and (b) different cutting depths.

Accordingly, the yield boundary within the workpiece can be determined by comparing the von Mises equivalent stress with the yield strength, and the depth of plastic deformation induced during the machining process can thus be quantified. Fig. 13(a) presents the calculated plastic deformation depth under different spindle speeds. It can be observed that the plastic deformation depth gradually decreases with increasing spindle speed, which is consistent with the variation trend of grinding force discussed in Section 3.2. An increase in spindle speed reduces the material removal volume per abrasive grain, thereby lowering the cutting force generated by material shearing. The reduction in cutting force decreases the contact load

between the abrasive grains and the workpiece, leading to a reduction in mechanical stress and, consequently, a shrinkage of the plastically deformed region within the material. From the stress contour maps, a more uniform stress distribution can also be observed. This behavior can be attributed to the change in heat source characteristics induced by increasing spindle speed, which in turn alters the distribution of thermal stress. Fig. 13(b) shows that increasing the grinding depth leads to a pronounced increase in the plastic deformation depth, whereas the overall shape of the stress distribution remains nearly unchanged. This is because a larger grinding depth directly increases both the normal and tangential grinding loads, resulting in higher mechanical and thermal stresses. Overall, the plastic deformation depth exhibits a strong correlation with the grinding force. This correlation arises because, throughout the grinding process, the grinding force not only directly governs the mechanical stress but also indirectly influences the distribution of the grinding heat source.

4.3. Microscopic mechanisms of RS formation under different loading conditions

In order to more accurately describe the distribution trend of subsurface RS, we fitted the relevant characteristic parameters based on experimental data. Fig. 19(a) shows the calculation process for subsurface RS distribution, with the characteristic parameters obtained through genetic algorithm fitting in equation (4). The corresponding characteristic parameters are shown in Table 3. By using the fitted parameters, the calculated plastic deformation depth, and the ρ_{GND} distribution along the depth direction, the subsurface RS distribution can be computed, and the RS distribution curve can be obtained by averaging the RS in the same horizontal direction.

As shown in Fig. 14(b) and (c), the calculated values of RS along the depth direction match well with the experimental data. In UVAEG, lower spindle speeds are beneficial for forming larger surface compressive RS and deeper compressive RS layers, which are closely related to the internal microstructural features. At lower spindle speeds, the increased material removal volume per grain leads to a higher grinding force exerted on the workpiece surface, resulting in relatively larger stress on the surface. Furthermore, due to the periodic impact effect of ultrasonic vibration, the number of impacts per grain at the same location increases at lower speeds, making the subsurface more prone to stress accumulation and transmission, which results in larger elastic strain within the material. From a microscopic perspective, the high stress generated at low spindle speeds promotes the proliferation and motion of surface dislocations.

At the same time, the lower cutting temperature inhibits dislocation annihilation and recovery, making the machined surface more likely to form higher dislocation density and deeper defect-affected layers. Upon the removal of external loads, the increased number of dislocations and defects intensifies the hindrance to the recovery of internal elastic deformation, leading to a greater amount of elastic strain being frozen inside the workpiece, resulting in larger compressive RS.

Table 3

Characteristic parameters

K_R	α_R	β_R	λ_R	ω_R
10.349	31.215	38.572	-14.861	0.012

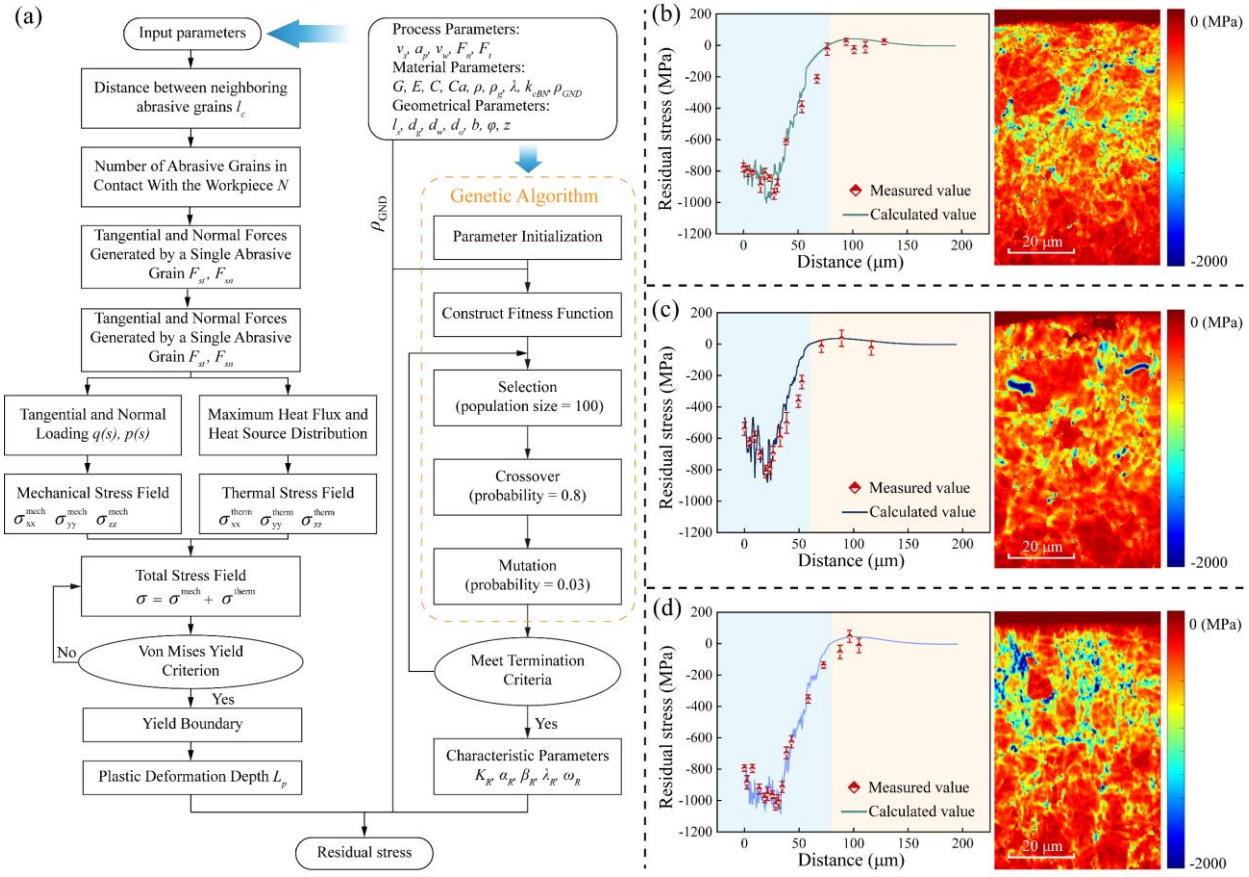


Fig. 14. Calculated results of residual stress: (a) calculation workflow; (b) residual stress distribution at a spindle speed of 2000 rpm and a cutting depth of 30 μm; (c) residual stress distribution at a spindle speed of 3000 rpm and a cutting depth of 30 μm; (d) residual stress distribution at a spindle speed of 2000 rpm and a cutting depth of 40 μm.

It is undeniable that RS does not continuously decrease with increasing spindle speed. Although the number of impacts per grain on the workpiece surface decreases with higher spindle speeds, an increase in spindle speed results in an increased strain rate of the material. When the strain rate increases to a certain extent, the hardening mechanisms produced by high strain rates far outweigh the material's thermal

softening mechanisms, leading to a reduction in dislocation emission and motion speeds. As a result, a higher dislocation density forms on the material surface, and the internal compressive RS may also increase. The increase in cutting depth also leads to an increase in internal RS (Fig. 14(d)), a phenomenon that is related to the changes in internal dislocations. A larger cutting depth means an increase in the material removal volume and grinding force per unit time, which in turn results in more severe plastic deformation within the material. This leads to an increased number of dislocations and other defects on the machined surface, strengthening the hindrance to the recovery of elastic strain, ultimately resulting in greater RS and deeper stress-affected layers within the material.

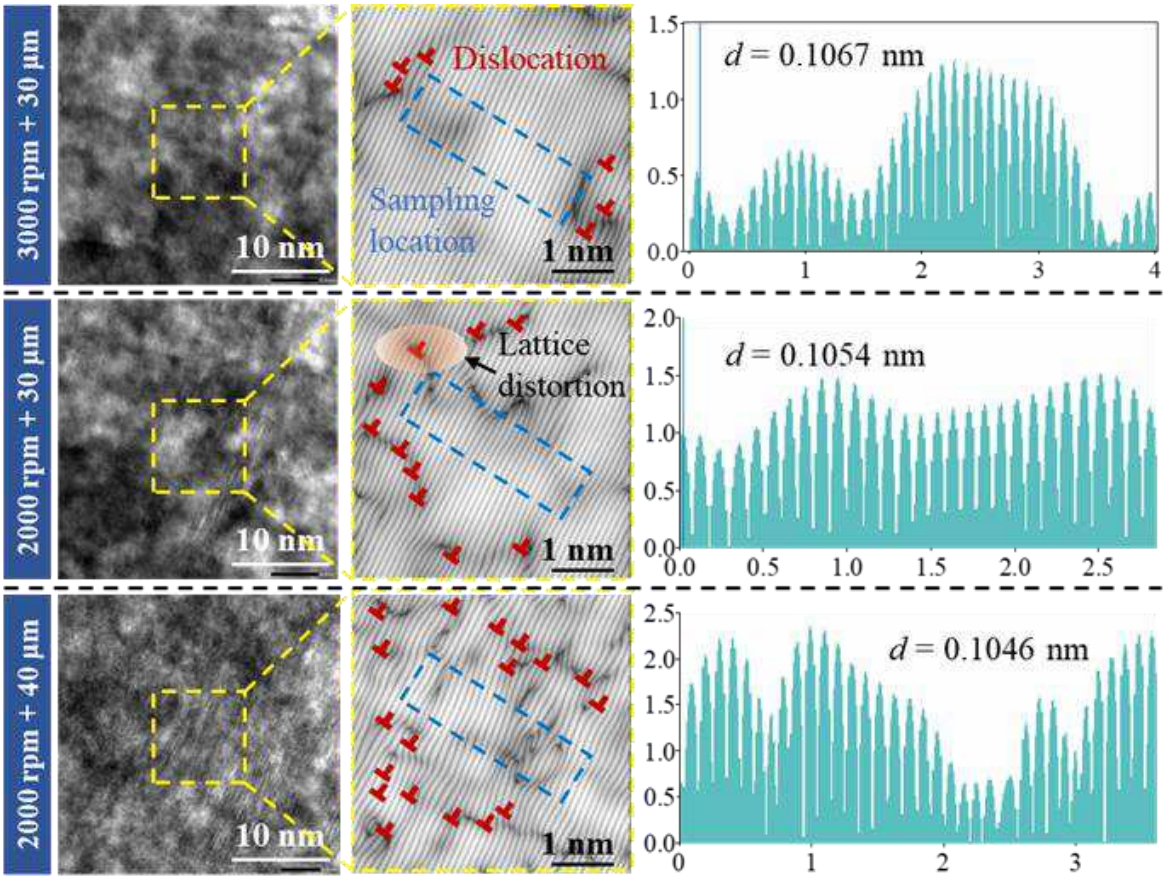


Fig. 15. Average interplanar spacing of the machined surface layer under different process parameters

Interplanar spacing can directly reflect the residual strain state of the machined surface layer. The magnitude of RS can be indirectly characterized through the strain–stress relationship. Fig. 15 shows the average interplanar spacing of the machined surface layer under different process parameters. At a rotational speed of 3000 rpm, a large number of dislocations are dispersed in the surface layer. Lattice distortion is observed around the dislocations. The average interplanar spacing is measured as 0.1067 nm based on lattice fringe analysis in the sampled region. When the rotational speed decreases to 2000 rpm, the

dislocation density is significantly increased. The dislocations evolve from a dispersed distribution to entangled and locally structured configurations. The average interplanar spacing is reduced to 0.1054 nm. When the cutting depth is further increased to 40 μm, the average interplanar spacing is further reduced to 0.1046 nm. These results directly reflect the variation in macroscopic RS induced by dislocation evolution. The rationality of the RS results in Fig. 4 and Fig. 14 is further supported. The introduction of dislocations produces local compressive lattice distortion through their elastic stress fields. Meanwhile, as the dislocation density increases, the interaction between dislocations is enhanced. The superposition of stress fields leads to a stable RS field at a larger scale.

5. Conclusion

In this study, the gradient RS, dislocation density and subsurface nanoscale substructures after UVAEG were systematically characterized. The variation of grinding force was monitored in situ. An evaluation method for the gradient RS on machined surfaces was proposed. A prediction model of gradient RS was established, considering material properties, dislocation density and plastic deformation depth. The inherent microscopic mechanism of RS was revealed from the microscale perspective. The main conclusions are as follows:

(1) The high-density dislocations introduced during UVAEG and their gradient distribution along the depth direction were confirmed as the dominant microscopic mechanism for the formation of surface compressive RS. The surface layer undergoes intense elastoplastic deformation under strong normal load and shear, rapidly decaying over a range of several microns to tens of microns, thus forming a distinct dislocation density gradient in the subsurface region.

(2) The plastic deformation depth directly controls the spatial scale of the dislocation-affected layer, thereby determining the penetration depth of the compressive RS layer. The depth of the compressive RS layer is of the same order of magnitude as the plastic deformation depth and increases simultaneously with the expansion of the dislocation density distribution range.

(3) The retained dislocations and their elastic stress fields significantly hinder the recovery of internal elastic strain in the material, allowing part of the elastic deformation to be retained and transformed into stable RS. Reducing the spindle speed and increasing the cutting depth increases the mechanical load on individual abrasive grains, promoting dislocation nucleation and accumulation, strengthening the hindrance to elastic strain recovery, and facilitating the formation of larger RS and stress-affected layers.

References

1. Ostergaard HE, Pribe JD, Hasib MT, et al (2025) Crack growth in laser powder bed fusion fabricated alloy 718 at 650 °C under static and cyclic loading. Int J Fatigue 193:108810. https://doi.org/10.1016/j.ijfatigue.2025.108810

2. Hosseini E, Popovich VA (2019) A review of mechanical properties of additively manufactured Inconel 718. Addit Manuf 30:100877. https://doi.org/10.1016/j.addma.2019.100877

3. Gong P, Zhang Y, Wang C, et al (2024) Residual stress generation in grinding: Mechanism and modeling. J Mater Process Technol 324:118262. https://doi.org/10.1016/j.jmatprotec.2023.118262

4. Tichoň D, Vojtek T, Jambor M, et al (2026) Fatigue life prediction of weld joints: Microstructural variation can be omitted while residual stress consideration is essential. Eng Fract Mech 331:111669. https://doi.org/10.1016/j.engfracmech.2025.111669

5. Soyama H, Eakins D, Korsunsky AM (2026) Importance of surface defect removal and compressive residual stress introduction in improving fatigue strength of powder bed-fused Ti6Al4V and demonstration of fatigue strength beyond that of hot-rolled Ti6Al4V. Int J Fatigue 203:109342. https://doi.org/10.1016/j.ijfatigue.2025.109342

6. Zhang X, Wei D, Liu X, et al (2025) Effect of compressive residual stress and surface morphology introduced by shot peening on the improvement of fretting fatigue life of TC4. Int J Fatigue 194:108835. https://doi.org/10.1016/j.ijfatigue.2025.108835

7. Benedetti M, Pedranz M, Fontanari V, et al (2024) Enhancing plain fatigue strength in aluminum alloys through shot peening: Experimental investigations and a strain energy density interpretation. Int J Fatigue 184:108299. https://doi.org/10.1016/j.ijfatigue.2024.108299

8. Ball DL, Ryan MA (2024) Uncertainty quantification in residual stress affected fatigue crack growth life. Int J Fatigue 189:108569. https://doi.org/10.1016/j.ijfatigue.2024.108569

9. Kim J, Hill MR (2023) Assessment of crack face contact using a weight function with application to fatigue crack growth in residual stress bearing bodies. Int J Fatigue 176:107858. https://doi.org/10.1016/j.ijfatigue.2023.107858

10. Shoemaker TK, Harris ZD, Smudde CM, et al (2023) 3D fatigue crack path deflection and residual stresses in 17-4PH stainless steel rod. Int J Fatigue 175:107735. https://doi.org/10.1016/j.ijfatigue.2023.107735

11. Zhang W, Fang K, Hu Y, et al (2016) Effect of machining-induced surface residual stress on initiation of stress corrosion cracking in 316 austenitic stainless steel. Corros Sci 108:173–184. https://doi.org/10.1016/j.corsci.2016.03.008

12. Turski M, Bouchard PJ, Steuwer A, Withers PJ (2008) Residual stress driven creep cracking in AISI Type 316 stainless steel. Acta Mater 56:3598–3612. https://doi.org/10.1016/j.actamat.2008.03.045

13. Singh A, Agrawal A (2015) Investigation of surface residual stress distribution in deformation machining process for aluminum alloy. J Mater Process Technol 225:195–202. https://doi.org/10.1016/j.jmatprotec.2015.05.025

14. Chen W, Voisin T, Zhang Y, et al (2019) Microscale residual stresses in additively manufactured stainless steel. Nat Commun 10:4338. https://doi.org/10.1038/s41467-019-12265-8

15. Almer JD, Cohen JB, Moran B (2000) The effects of residual macrostresses and microstresses on fatigue crack initiation. Mater Sci Eng A 284:268–279. https://doi.org/10.1016/S0921-5093(99)00779-0

16. Hong Y, Wang C, Wang L, et al (2024) Characterization of microscopic residual stresses: A review. Eng Fract Mech 310:110441. https://doi.org/10.1016/j.engfracmech.2024.110441

17. Hong Y, Wang C, Wang L, et al (2024) Characterization of microscopic residual stresses: A review. Eng Fract Mech 310:110441. https://doi.org/10.1016/j.engfracmech.2024.110441

18. Zhang XX, Ni DR, Xiao BL, et al (2015) Determination of macroscopic and microscopic residual stresses in friction stir welded metal matrix composites via neutron diffraction. Acta Mater 87:161–173. https://doi.org/10.1016/j.actamat.2015.01.006

19. Chandroth AM, Prabhu N, Diehl M, et al (2026) Effect of local crystallographic texture on near-surface residual stress variation in machined titanium. J Mater Process Technol 347:119153. https://doi.org/10.1016/j.jmatprotec.2025.119153

20. Dye D, Stone HJ, Reed RC (2001) Intergranular and interphase microstresses. Curr Opin Solid State Mater Sci 5:31–37. https://doi.org/10.1016/S1359-0286(00)00019-X

21. Gu LM, Zhang J, Liu Y, et al (2026) Macroscopic and microscopic residual stress relief in SiC/Al composites: Effects of annealing and cryogenic treatment. J Mater Sci Technol 254:106–116. https://doi.org/10.1016/j.jmst.2025.08.013

22. Zhang B, Gao G, Li R, et al (2026) Study on residual stress of 1J22 alloy in longitudinal-torsional ultrasonic milling: modeling and multi-scale simulation. Eur J Mech - ASolids 116:105898. https://doi.org/10.1016/j.euromechsol.2025.105898

23. Zhang S, Shi H, Qi J, et al (2025) Prediction of residual stress in milling large or medium-sized thin-walled parts based on equivalent loads. J Manuf Process 151:282–297. https://doi.org/10.1016/j.jmapro.2025.05.079

24. Ma J, Liu Y, Zhao Y, et al (2025) A novel analytical model for predicting the thin-walled workpiece deformation considering the effect of residual stress accumulation and redistribution in layer by layer milling. J Manuf Process 141:1444–1462. https://doi.org/10.1016/j.jmapro.2025.03.018

25. Yao G, Liu Z (2024) Analytical modelling for residual stress prediction in multi-step side milling of GH4169 thin-wall parts based on deformation. J Mater Res Technol 32:1984–1995. https://doi.org/10.1016/j.jmrt.2024.08.042

26. Chen Z, Qian L, Du J, et al (2024) A novel method to predict residual stress by coupling the phase transition effect for LA103Z Mg-Li alloy milling. J Manuf Process 124:936–953. https://doi.org/10.1016/j.jmapro.2024.06.057

27. Zeng H, Hu X, Yang D (2023) Analytical modeling of residual stresses in laser-assisted milling AerMet100 steel. Opt Laser Technol 158:108931. https://doi.org/10.1016/j.optlastec.2022.108931

28. Malkin S, Guo C (2007) Thermal Analysis of Grinding. CIRP Ann 56:760–782. https://doi.org/10.1016/j.cirp.2007.10.005

29. Ding Z, Sun G, Guo M, et al (2020) Effect of phase transition on micro-grinding-induced residual stress. J Mater Process Technol 281:116647. https://doi.org/10.1016/j.jmatprotec.2020.116647

30. Li G, Liu J, Wang H, et al (2025) Residual stress and subsurface damage prediction in tungsten heavy alloy face grinding. J Manuf Process 134:175–192. https://doi.org/10.1016/j.jmapro.2024.12.038

31. Ballard P, Fournier J, Fabbro R, Frelat J (1991) RESIDUAL STRESSES INDUCED BY LASER-SHOCKS. J Phys IV 01:C3-487-C3-494. https://doi.org/10.1051/jp4:1991369

32. Da Silva FAV, Franzão HS, Outeiro JC (2025) Prediction of the energy consumption and surface integrity in machining of Inconel 718 superalloy using an orthogonal cutting model considering the stress state. J Manuf Process 149:82–97. https://doi.org/10.1016/j.jmapro.2025.05.038

33. Jiang X, Sun N, Ren F, et al (2026) Multi-process aerospace components: Residual stress modeling and deformation optimization. Int J Mech Sci 309:111077. https://doi.org/10.1016/j.ijmecsci.2025.111077

34. Xu Y, Gong Y, Zhang W, et al (2022) Microstructure evolution and dynamic recrystallization mechanism induced by grinding of Ni-based single crystal superalloy. J Mater Process Technol 310:117784. https://doi.org/10.1016/j.jmatprotec.2022.117784

35. Jiang Q, He B, Li S, et al (2025) Hierarchically ultrafine grains with the embedded nanotwins structure produced in ultra-high strain rate deformation of coarse-grained titanium alloy. J Mater Process Technol 345:119070. https://doi.org/10.1016/j.jmatprotec.2025.119070

36. Su Y, Oikawa K, Shinohara T, et al (2023) Residual stress relaxation by bending fatigue in induction-hardened gear studied by neutron Bragg edge transmission imaging and X-ray diffraction. Int J Fatigue 174:107729. https://doi.org/10.1016/j.ijfatigue.2023.107729

37. Akbari M, Buhl S, Leinenbach C, Wegener K (2016) A new value for Johnson Cook damage limit criterion in machining with large negative rake angle as basis for understanding of grinding. J Mater Process Technol 234:58–71. https://doi.org/10.1016/j.jmatprotec.2016.03.009

38. Lubarda VA, Kouris DA (1996) Stress fields due to dislocation arrays at interfaces. Mech Mater 23:191–203. https://doi.org/10.1016/0167-6636(96)00008-7

39. An D, Liu X, Xiao Y, et al (2025) Correlating the evolution of spatial-resolved microscale residual

stress and the associated dislocation behavior in additively manufactured 316L stainless steel upon short-term annealing. Addit Manuf 106:104807. https://doi.org/10.1016/j.addma.2025.104807

40. Liu S, Ding Z, Li M, et al (2026) Investigations on residual stress of size effect in multi-pass precision milling of titanium alloy: Experiments and modeling. J Manuf Process 166:1–20. https://doi.org/10.1016/j.jmapro.2026.03.033

41. Zhang D, Mao C, Hu Y, et al (2025) Microstructure evolution and nanocrystallization mechanism induced by grinding of hardened AISI 52100 steel. J Mater Process Technol 341:118909. https://doi.org/10.1016/j.jmatprotec.2025.118909

42. Yao L, Liu Z, Song Q, et al (2023) Prediction modelling of cutting force in rotary ultrasonic end grinding 2.5D woven SiO2f/SiO2 ceramic matrix composite. Compos Struct 304:116448. https://doi.org/10.1016/j.compstruct.2022.116448

43. Zhao M, Mao J, Ji X, et al (2021) Effect of crystallographic orientation on residual stress induced in micro-grinding. Int J Adv Manuf Technol 112:1271–1284. https://doi.org/10.1007/s00170-020-06329-z

44. Ye S, Wen J, Tang J, et al (2024) Calculation of residual stress in ultrasonic vibration assisted grinding considering thermal-mechanical coupling: a numerical-analytical hybrid prediction approach. Mech Time-Depend Mater 28:2981–3003. https://doi.org/10.1007/s11043-024-09707-2

45. Zhao M, Mao J, Ji X, et al (2021) Effect of crystallographic orientation on residual stress induced in micro-grinding. Int J Adv Manuf Technol 112:1271–1284. https://doi.org/10.1007/s00170-020-06329-z

46. Yao Y, Sun C, Xiu S, et al (2022) Study on dynamic recrystallization-based microstructure evolution mechanism of 40Cr during strengthening grinding. J Mater Process Technol 309:117754. https://doi.org/10.1016/j.jmatprotec.2022.117754

47. Gong P, Zhang Y, Wang C, et al (2024) Residual stress generation in grinding: Mechanism and modeling. J Mater Process Technol 324:118262. https://doi.org/10.1016/j.jmatprotec.2023.118262

48. Sun S, Yue C, Liu X, et al (2025) Analytical modeling of milling induced residual stress based on feed per tooth. J Manuf Process 155:504–521. https://doi.org/10.1016/j.jmapro.2025.09.079

49. Donato GHB, Bianchi M (2011) Numerical modeling of uneven thermoplastic polymers behaviour using experimental stress-strain data and pressure dependent von Mises yield criteria to improve design practices. Procedia Eng 10:1871–1876. https://doi.org/10.1016/j.proeng.2011.04.311

Acknowledgements

This study was supported by the National Science Fund for Distinguished Young Scholars (No. 52325506)

Declaration of competing interest

The authors declare that they have no known competing financial interests or personal relationships that could have appeared to influence the work reported in this paper.

Data availability

Data will be made available on request.